Depth of Sudden Velocity Changes Derived From Multi-Mode Rayleigh Waves

Finger, C.; Löer, K.

Important note
To cite this publication, please use the final published version (if applicable).
Please check the document version above.

Correspondence to:

C. Finger,
claudia.finger@ieg.fraunhofer.de

Author Contributions:

Conceptualization: C. Finger, K. Löer
Data curation: C. Finger
Formal analysis: C. Finger, K. Löer
Investigation: C. Finger, K. Löer
Methodology: C. Finger, K. Löer
Resources: C. Finger
Software: C. Finger, K. Löer
Supervision: K. Löer
Validation: C. Finger, K. Löer
Visualization: C. Finger
Writing – original draft: C. Finger
Writing – review & editing: C. Finger, K. Löer

Depth of Sudden Velocity Changes Derived From Multi-Mode Rayleigh Waves

C. Finger[1] and K. Löer[2,3]

[1]Fraunhofer IEG, Fraunhofer Institution for Energy Infrastructures and Geothermal Systems, Zittau, Germany, [2]School of Geosciences, University of Aberdeen, Aberdeen, Scotland, [3]Now at Department of Geoscience & Engineering, TU Delft, Delft, The Netherlands

Abstract To integrate structural subsurface models and smooth seismic velocity models, they need to share common features and resolutions. Here, we propose a new approach, Depth Assessment from Rayleigh Wave Ellipticities (DARE), for estimating the depth of sudden velocity changes from ambient-noise multi-mode Rayleigh waves applicable to a wide range of frequencies. At frequencies where multi-mode Rayleigh waves have an extremum in ellipticity, the phase velocity can be used to estimate the depth of sudden velocity changes. We test our approach theoretically, numerically, and on real data from two geothermal sites by extracting Rayleigh wave ellipticities and phase velocities from three-component beamforming of ambient noise using the python code package B3AMpy. For a small-scale array, our approach validates the depth of quaternary sediments predicted by geological models. For deeper velocity changes, high uncertainties remain but the general trend of inclining boundaries can be recovered well. We demonstrate that, if impedance contrasts are larger than three, our approach is valid for multiple layers, laterally heterogeneous models, and a wide range of Poisson ratios.

Plain Language Summary To effectively combine structural models and seismic velocity models, we've developed a new method. It estimates the depth of sudden changes in seismic velocity using Rayleigh waves from ambient noise. By identifying minima and maxima in Rayleigh wave ellipticity, we determine the depth of sudden velocity changes from the observed phase velocity at that point. We tested the method and found it works well for various scenarios, including multiple layers, heterogeneous models, and different material properties. This new Rayleigh wave method could be useful in seismic hazard studies to determine the depth of sedimentary basins.

1. Introduction

Accurate representations of the subsurface are crucial for exploring natural resources, such as geothermal or hydrocarbon reservoirs, and estimating associated risks. Subsurface geophysical models can be structural, that is, containing locations of faults and discontinuities, or represent a smooth spatial distribution of properties, that is, as in seismic velocity models. Information from both types of models are crucial to estimate the extent of reservoirs, needed to evaluate their economic viability, and accurately locating (micro-) seismicity to estimate and monitor the seismic hazard. Thus, structural and velocity models should ultimately be integrated into a common subsurface model that simultaneously includes smooth variations and sudden changes of elastic properties. Here, we introduce a novel approach, Depth Assessment from Rayleigh Wave Ellipticities (DARE), that retrieves structural information, that is, the depth of sudden velocity changes, from ambient seismic noise recordings. DARE has the potential to serve as boundary conditions for future inversions of dispersion curves and, thus, bridge the gap between structural and overly smoothed models.

Active seismic surveys are widely used to obtain high-resolution structural models but are challenged by high costs and permitting issues, especially in urban areas. Tomographic velocity models developed from earthquake data can be used to constrain seismic velocities between hypocenters and seismic stations but require an adequate distribution of local seismic events to fully illuminate the subsurface (Toledo et al., 2020). Ambient seismic noise methods can image the subsurface regardless of the local seismicity level and without the need for active seismic sources. Although body waves have recently been identified in ambient noise recordings (Brenguier et al., 2019; Nakata et al., 2015), most studies invert velocity profiles from surface wave dispersion curves (Galetti et al., 2017; Löer et al., 2020). However, the large wavelengths of low-frequency surface waves increase uncertainties at

greater depths and result in smooth and gradient-like velocity models that lack sharp features. Thus, integration of active and passive methods is challenging due to different geometries, different frequencies, and a lack in common features to validate the integration. In this study, we aim to close the gap between active and passive subsurface models by retrieving structural information, that is, the depth of major sudden velocity changes, from ambient noise Rayleigh waves. In contrast to other methods, such as horizontal-to-vertical spectral ratios (HVSR; Bonnefoy-Claudet et al., 2006), DARE does not rely on velocity information from secondary studies and does not make prior assumptions about the wave types in seismic recordings. No inversion is needed to determine a preliminary depth estimate using DARE.

Several studies jointly inverted Rayleigh wave phase velocities and ellipticities for shallow (Picozzi et al., 2005) and deep (Berg et al., 2018) velocity models. If Rayleigh waves dominate the analyzed frequency range, the HVSR curve closely resembles Rayleigh wave ellipticities (Fäh et al., 2008). The peak frequency of HVSR together with an estimate of the average shear velocity of the sediments can be used to estimate the thickness of sediments overlaying a stiffer bedrock, if the impedance contrast is larger than three (Bard & Team, 2004; Bonnefoy-Claudet et al., 2006). However, the accuracy of the depth estimate of HVSR strongly relies on accurate estimates of the shear-wave velocity. Since HVSR is typically applied to short recordings from single surface stations, sensitivity is in practice often limited to frequency ranges above 0.1 Hz and, thus, is limited to depths of about one hundred meters. It is assumed that the subsurface can be represented with a one-dimensional velocity profile. Rayleigh wave ellipticities retrieved from single station recordings (HVSR; Bonnefoy-Claudet et al., 2006) and ambient-noise cross-correlations (Berg et al., 2018; Lin et al., 2012) are challenged by mis-identifying wave types and modes. Thus, there is a need for a method that does not inherently assume the dominance of Rayleigh waves and works in a larger frequency range to image larger depth ranges.

In this study, we propose a new method, DARE, to estimate the depth of sudden velocity changes whenever phase velocity and ellipticity can be resolved over the same frequency range. At frequencies where multi-mode Rayleigh wave ellipticities have a minimum or maximum value, the phase velocity can be used together with the frequency to estimate the depth of a velocity increase. We validate DARE using analytical approximations and a variety of one-dimensional velocity models. Three-component (3C) ambient noise beamforming at multiple seismic stations provides phase velocity and ellipticity of retrograde and prograde Rayleigh waves. We use the python code package B3AMpy (Finger & Löer, 2023; Löer et al., 2023) to perform 3C beamforming. The depth sensitivity depends mainly on the array geometry. We demonstrate the application of DARE by applying 3C beamforming to synthetic waveforms and recorded waveforms from three seismic arrays at two sites. We find good agreement between our depth estimates and available depth estimates from active surveys and geological models. The accuracy of DARE is comparable to HVSR results assuming the shear-wave velocity is perfectly known. However, DARE is applicable to a wider depth range than HVSR and works without prior assumptions or input from secondary studies.

2. Estimating the Depth of Sudden Velocity Changes Using Rayleigh Waves

Rayleigh waves at different frequencies are sensitive to different depths. If seismic velocities vary as a function of depth, this becomes evident in the dispersive behavior of Rayleigh waves, which describes the variation of their velocity with frequency. Low-frequency waves tend to have larger wavelengths and hence sample larger depth. Assuming that there is a velocity contrast in the subsurface, it follows that Rayleigh waves at certain frequencies are more sensitive to this contrast than others, depending on the depth of the contrast. This fact is exploited by dispersion curve inversion techniques (e.g., Socco & Strobbia, 2004), which convert velocity-frequency measurements into velocity-depth profiles by iteratively forward-modeling and evaluating dispersion curves. However, these techniques are computationally expensive, require an initial guess of the velocity distribution, and can result in non-unique solutions that are challenging to interpret geologically (Tsai et al., 2023).

For a quicker and computationally cheaper analysis of velocity contrasts, we suggest exploiting another feature of Rayleigh wave dispersion: not only does the velocity change with frequency but also the ellipticity of the Rayleigh wave, that is, the ratio of horizontal to vertical particle motion. Hence, the depth of a velocity discontinuity also affects the shape of an ellipticity curve (Boaga et al., 2013). Additionally, we make use of multiple modes of Rayleigh waves that coexist in the same medium, albeit at different frequencies, velocities, and ellipticities. We observe that for both fundamental (superscript 0) and first higher mode (superscript 1) frequencies at extreme ellipticities (f_p) can be related to the depth d of the velocity contrast according to
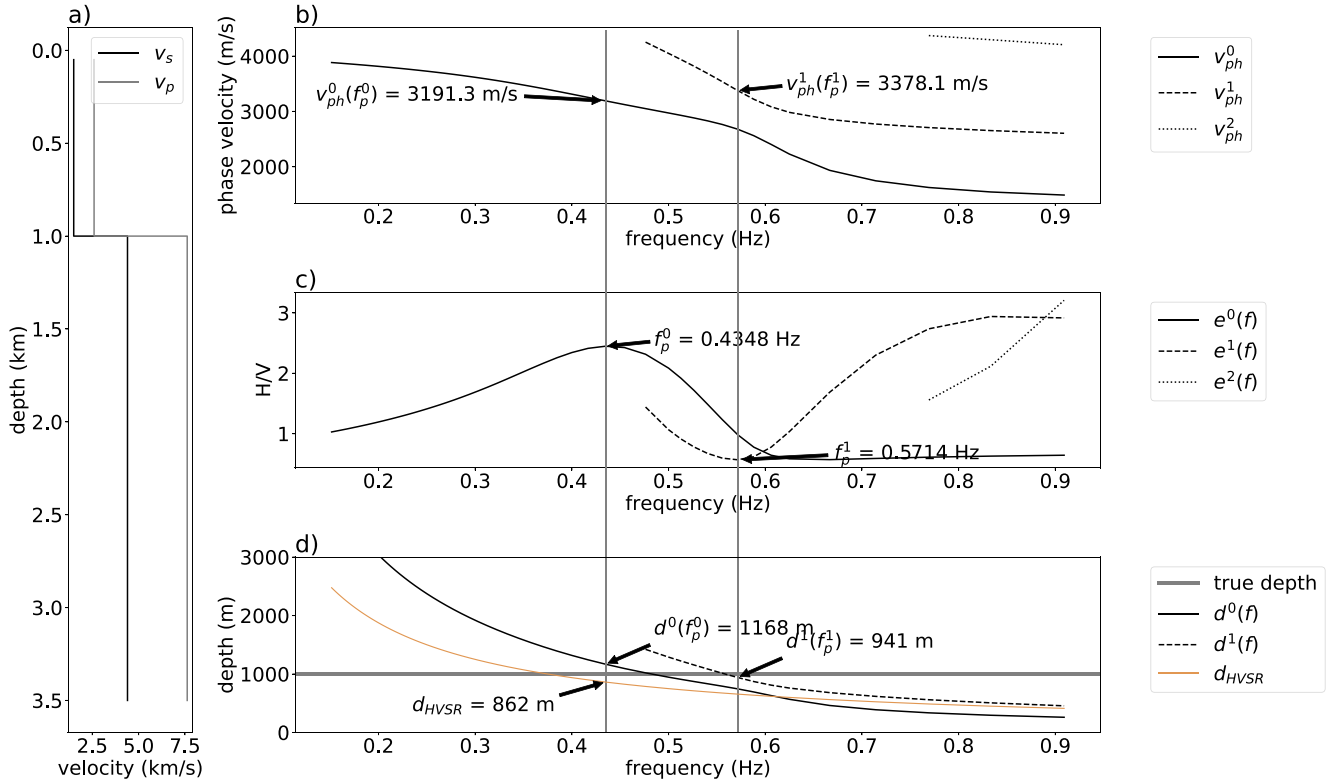
Figure 1. (a) Input one-dimensional velocity model for analytical approximation of multi-mode Rayleigh wave (b) phase velocity v_{ph} and (c) ellipticity $e = \frac{H}{V}$ using CPS (Herrmann, 2013). (d) d^0 and d^1 calculated from (b) and (c) using Equations 1 and 2. The empirical relation d_{HVSR} (Equation 3), typically used in HVSR studies is plotted for comparison. Vertical gray lines show frequencies where the fundamental and first higher mode experience extrema in ellipticity.

$$d^0 = \frac{v_{ph}^0\left(f_p^0\right)}{2\pi f_p^0}, \tag{1}$$

or

$$d^1 = \frac{v_{ph}^1\left(f_p^1\right)}{2\pi f_p^1}, \tag{2}$$

where $v_{ph}^0\left(f_p^0\right)$ and $v_{ph}^1\left(f_p^1\right)$ are fundamental and first higher mode phase velocities, respectively, at frequencies of extreme ellipticity. Figure 1 shows an example for a one-dimensional velocity profile, where v_{ph} and were estimated using Computer Programs in Seismology (CPS; Herrmann, 2013). For a two-layer velocity model with a sudden velocity increase in a depth of $d = 1$ km and $\frac{v_p}{v_s} = \sqrt{3}$ (Figure 1a), v_{ph} and $e = \frac{H}{V}$ are shown in Figures 1b and 1c, respectively, for both fundamental and the first higher mode. Using Equations 1 and 2, the depth of the velocity contrast is calculated (Figure 1d). The depth estimates obtained from the fundamental and first higher mode are in this case $d^0 = 1,168$ m and $d^1 = 941$ m, respectively. Since Equation 1 over-estimates and Equation 2 under-estimates the depth of the contrast, the most accurate result is in fact obtained from the average of d^0 and d^1, which gives 1,054.5 m, a deviation of 5.5% from the true depth. Note that the depth estimate using the first higher mode is slightly more accurate than the one using the fundamental mode only. Therefore, if the first higher mode can be retrieved reliably, it should be preferred over the fundamental mode.

For comparison, we calculate the depth of the contrast from the empirical relation typically used in HVSR studies (Bonnefoy-Claudet et al., 2006)
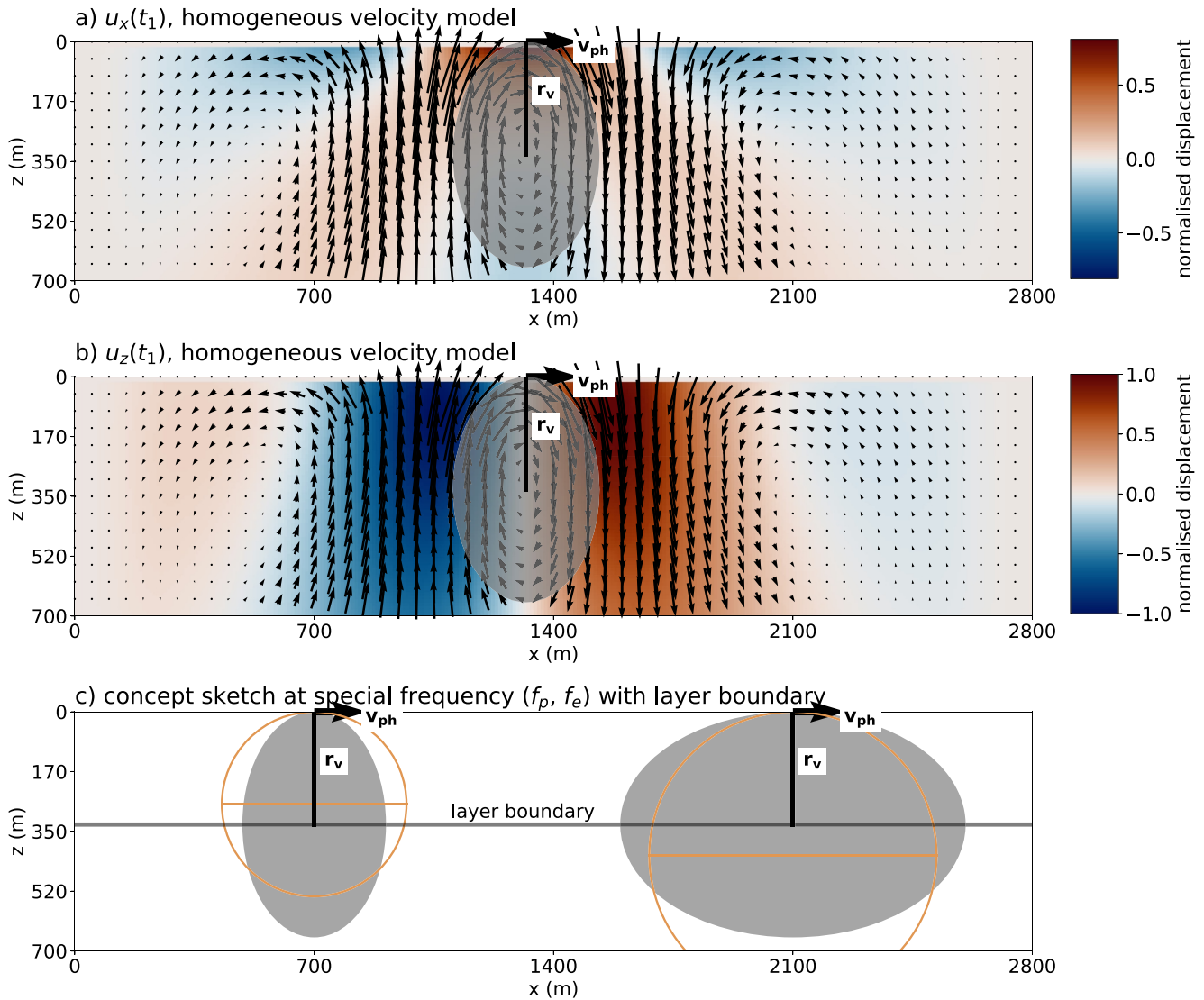
Figure 2. Snapshots of displacement in (a) x direction and (b) z direction for a Rayleigh wave propagating in positive x direction in a homogeneous velocity model. Snapshots were created with a rotated staggered-grid finite difference scheme (Saenger et al., 2000). Energy ellipse is shaded gray. (c) Sketch illustrating the estimation of the depth of a layer boundary as the half height of ellipses using the auxiliary circle (orange).

$$d_{HVSR} = \frac{v_s^1}{4 f_{max}^0},$$ (3)

where v_s^1 is the shear-wave velocity in the upper layer and f_{max}^0 the frequency at which the H/V ratio has a maximum (here equivalent to the maximum ellipticity of the fundamental mode). Assuming that $v_s^1 = 1500 \, \text{m/s}$ is known, this results in an estimate of $d_{HVSR} = 862 \, \text{m}$, a deviation of more than 10 %. Thus, in this case DARE is more accurate than HVSR.

Attempting a physical interpretation of the new empirical relationship (Equations 1 and 2), we study Rayleigh wave motion in a two-dimensional wave-propagation model (Figure 2): In homogeneous Poisson media, Rayleigh wave motion is elliptical and retrograde at the surface and inverts to prograde motion at greater depths. A particle at the surface is displaced in vertical and horizontal direction with peak motions shifted in phase by $\frac{\pi}{2}$. The ellipticity $e = \frac{H}{V}$ is smaller than one in homogeneous Poisson solids. The energy of a passing Rayleigh wave induces the displacement of all particles in a subvolume. The two-dimensional snapshots of the displacement

wavefield (Figures 2a and 2b) show that the displacement describes an elliptical motion with an ellipticity similar to the particle motion at the surface. We refer to this as the *energy ellipse*. In the following, we show how the size and shape of this energy ellipse can be calculated using the horizontal propagation velocity, that is, the phase velocity v_{ph}, and frequency f of the Rayleigh wave, and how the size of the ellipse relates in fact to the depth of the velocity contrast computed in Equations 1 and 2.

We equate the wavelength $\lambda_R = \frac{v_{ph}}{f}$ of a Rayleigh wave to the circumference of the energy ellipse, approximated as $C_e = \pi\sqrt{2(r_v^2 + r_h^2)}$, where r_v and r_h are the length of the major and minor half-axis of the ellipse, respectively, yielding

$$\frac{v_{ph}}{f} = \pi\sqrt{2(r_v^2 + r_h^2)}. \tag{4}$$

For both vertical and horizontal ellipses (Figure 2c) r_v is the vertical half axis and ellipticity can be expressed as $e = \frac{r_h}{r_v}$. Substituting $r_h = er_v$ and solving Equation 4 for r_v gives

$$r_v = \frac{v_{ph}}{2\pi f}\sqrt{\frac{2}{1 + e^2}}. \tag{5}$$

Evaluating Equation 5 at the critical frequency $f = f_p^0$ for which e has a maximum and comparing it to Equation 1 that estimates the depth of the impedance contrast from the fundamental mode, we find that the only difference is the factor $\sqrt{\frac{2}{1+e^2}}$ that accounts for the actual ellipticity at f_p^0:

$$r_v\left(f_p^0\right) = \frac{v_{ph}\left(f_p^0\right)}{2\pi f_p^0}\sqrt{\frac{2}{1 + e\left(f_p^0\right)^2}} = d^0\sqrt{\frac{2}{1 + e\left(f_p^0\right)^2}} \tag{6}$$

Our formula for d^0 (Equation 1) is in fact an approximation of Equation 5 that neglects the absolute value of e, describing instead an auxiliary circle ($e = 1$) with the same circumference (orange circles in Figure 2c). For a horizontally polarized ellipse ($e > 1$), the factor $\sqrt{\frac{2}{1+e^2}} < 1$ meaning that $r_v < d^0$, hence, we would expect the depth to be overestimated, which is what we observe in 1d (see also Figure 2c, right circle/ellipse). For a vertically polarized ellipse (first higher mode at f_p^1) the opposite is the case, which justifies taking the average of both estimates. Note that in practice, e is often not well resolved over broad frequency ranges and absolute values have large uncertainties. Thus, using the auxiliary circle to estimate the half-height of the energy ellipse r_v (and thus the depth d) without explicitly using e is in fact a practical solution.

The sensitivity of the energy ellipse to the impedance contrast can be understood by investigating the dispersive behavior of Rayleigh wave ellipticity for both fundamental and first higher mode: At high frequencies, the fundamental mode (mode 0) is polarized vertically $\left(\frac{H}{V} < 1\right)$ and both r_v and $r_h = er_v$ are smaller than the depth of the sudden velocity increase, $r_v > r_h \ll d$ (Figure 1d). With decreasing frequency, the radii increase with different rates until they have equal length, $r_h = r_v$, $e = 1$, here at $f_e^0 = f_p^1 = 0.57$ Hz, where f_e^0 is the frequency where the fundamental mode Rayleigh wave has an ellipticity of one and f_p^1 is the frequency where the first higher mode has a minimum in ellipticity. The deeper part of the Rayleigh wave already "sees" the higher velocities at greater depths which causes different growth rates for r_v and r_h. For lower frequencies, $f < f_e^0$, one radius is larger than the depth of the velocity increase and the other is smaller than the depth of the velocity increase. If the shear velocity of the bottom layer is larger than the compressional velocity of the top layer, the ellipse changes to being horizontally polarized, $r_v < r_h$ (cf. Figure 2c right horizontal ellipse). The two radii then increase at different rates for decreasing frequencies until r_v is equal to the depth of the sudden velocity increase, $r_v = d$ (Figure 1d). At this frequency, here at $f_p^0 = 0.43$ Hz, where e of the fundamental mode has reached its maximum, r_v is about equal to the depth of the sudden velocity increase. At even smaller frequencies, the radius of the second circle is larger than d and "sees" the bottom layer velocities as well. e is declining again until the sensitivity of the energy ellipse is mostly to the deeper layer.
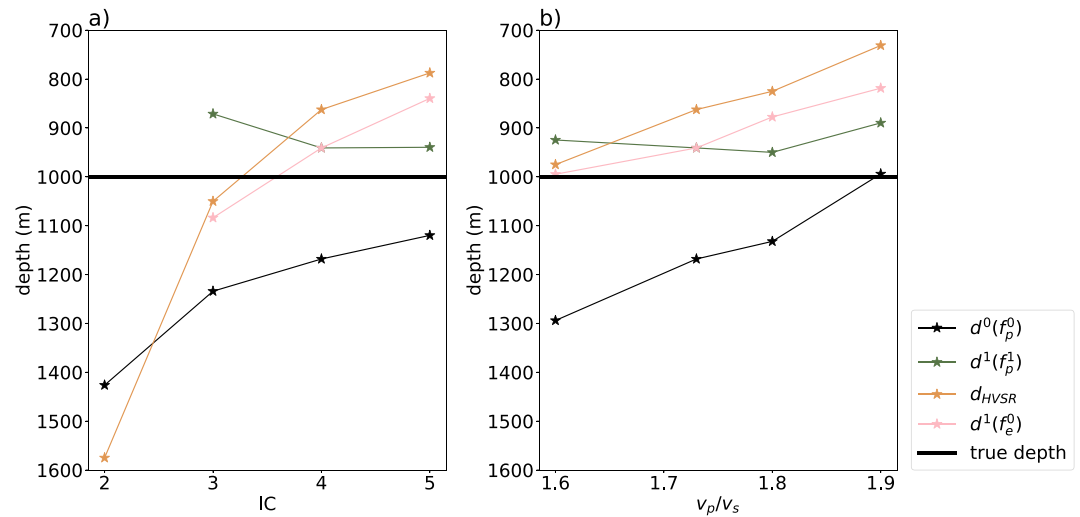
Figure 3. Depth estimates from DARE (d^0, d^1, and $d^1(f_e^0)$) and HVSR (d_{HVSR}) compared to the true depth for a range of one-dimensional two-layer models with (a) varying impedance contrasts but keeping the $\frac{v_p}{v_s}$-ratio constant at $\sqrt{3}$ and (b) varying the $\frac{v_p}{v_s}$-ratio but keeping the impedance contrast constant at four.

For the first higher mode (mode 1), a similar change can be observed (Figure 1d). The first higher mode is horizontally polarized for high frequencies with r_h being larger than the depth of the interface and r_v being smaller. With decreasing frequencies, r_v becomes as large as the depth of the sudden velocity increase with e being minimal, here at $f_p^1 = 0.57$ Hz. Thus, we can also infer d from the first higher mode Rayleigh wave using Equation 2 and the frequency f_p^1 where e of the first higher mode has a minimum. Note that in this case, the frequency where the fundamental mode Rayleigh wave is circular ($e = 0$) is equal to the frequency where the first higher mode has its minimum ellipticity ($f_p^1 = f_e^0$). Thus, if the ellipticity of the first higher mode cannot be retrieved, and f_p^1 not determined, the frequency f_e^0 seems to be a useful approximation of f_p^1 and still allows to use the wavenumber of the first higher mode. However, for more complex velocity models, f_p^1 and f_e^0 may not coincide as illustrated in the following analytical examples.

DARE relies on the existence of horizontally polarized Rayleigh waves and works best if the first higher mode of Rayleigh waves exists at investigated frequencies. As described above, the fundamental Rayleigh wave becomes horizontally polarized when the shear-wave velocity of the bottom layer is larger than the compressional-wave velocity of the shallower layer, $v_s^2 > v_p^1$. Assuming a Poisson solid, that is, $\frac{v_p}{v_s} = \sqrt{3}$, and densities of sandstone (about $\rho^1 = 2$ g/cm^3) and granite (about $\rho^2 = 2.63$ g/cm^3), the shear wave impedance contrast, $IC = \frac{\rho^2 v_s^2}{\rho^1 v_s^1}$ needs to be larger than 2.77 for v_s^2 to be larger than v_p^1. In our example velocity model (Figure 1), the impedance contrast is four. For HVSR studies, a minimum impedance contrast of three is typically reported (Bonnefoy-Claudet et al., 2006). We tested different IC by changing v_s^2 (Figure 3a). For $IC = 2$ the first higher mode does not exist at lower frequencies (Figure A1) and the peak in ellipticity of the fundamental mode is very small. Thus, the uncertainty of picking f_p^0 is high in this case and the deviation from the true source depth is high. We conclude that our method is valid for impedance contrasts larger than three. Note that only for $IC = 4$ is $r_v^1(f_p^1) = r_v^1(f_e^0)$ (Figure A1). An average from both modes would result in the most accurate depth estimate.

In the presence of fluids, the $\frac{v_p}{v_s}$-ratio can increase. Testing different $\frac{v_p}{v_s}$-ratios for both layers and using a constant impedance contrast of four reveals that with increasing $\frac{v_p}{v_s}$-ratio the phase velocities of the two modes become closer and mode mis-identification becomes more likely (Figure A1). The frequency where the velocities of the two modes are closest together is very close to $f_e^0 = f_p^1$. This frequency is also referred to as the osculation frequency (Boaga et al., 2013). We can estimate the true depth of the sudden velocity increase relatively well for
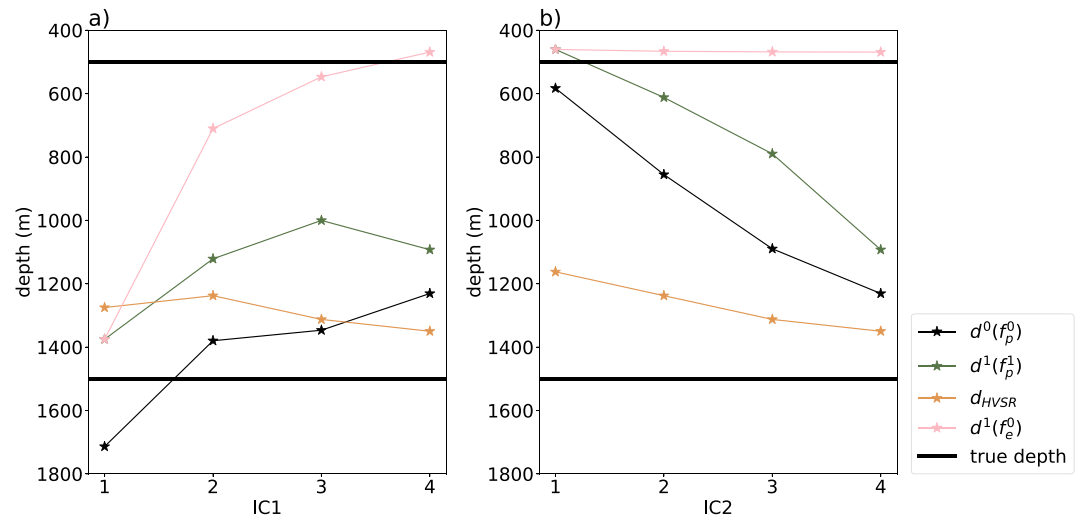
Figure 4. Depth estimates from DARE (d^0, d^1, and $d^1(f_e^0)$) and HVSR (d_{HVSR}) compared to the true depth for a range of one-dimensional three-layer models with a constant $\frac{v_p}{v_s}$-ratio of $\sqrt{3}$ but (a) varying the impedance contrast of the shallower velocity increase (IC1) but keeping the impedance contrast of the deeper increase constant at four (IC2 = 4) and (b) varying the impedance contrast of the deeper velocity increase (IC2) but keeping the impedance contrast of the shallower increase constant at four (IC1 = 4).

all tested $\frac{v_p}{v_s}$-ratios (Figure 3b). Note that also in these cases, the first higher mode provides more accurate depth estimates for a wider range of models than the fundamental mode and the depth estimate from HVSR.

Adding an additional layer with varying impedance contrasts to the one-dimensional models reveals that DARE tends to retrieve the stronger impedance contrast (Figure 4). If the stronger impedance contrast is deeper (Figure 4a), $r_v^1(f_e^0)$ retrieves the stronger shallower contrast if the impedance contrast is larger than three. If the stronger impedance contrast is shallower (Figure 4b), the shallower layer boundary can be retrieved accurately using $r_v^1(f_e^0)$ for all tested impedance contrasts. If the impedance contrasts at both depths are the same ($IC = 4$), the depth estimate is closer to the deeper impedance contrast. Low velocity zones can occur and are thus an important consideration. Reducing the velocity of the middle layer (not shown), reveals that deviations from the true depth are higher but a rough estimate of the depth of the larger, in our case deeper, velocity increase is still possible.

3. Three-Component Ambient-Noise Beamforming of Rayleigh Waves

To estimate the depth of sudden velocity increases using Equations 1 and 2, we need to estimate v_{ph} and e over the desired frequency range. We choose Beamforming of three-component ambient noise (B3AM; Löer et al., 2023) for its distinct advantages of identifying wave types in small time windows of continuous waveforms and producing v_{ph} and e at the same discrete frequencies. Results from all processed time windows can be analyzed statistically to obtain v_{ph} and e against frequency averaged over longer time windows. B3AM processes three-component waveforms recorded with multiple seismic stations and enables to identify prograde and retrograde Rayleigh waves separately, which allows a first indication of mode separation.

B3AM compares observed three-component phase shifts S^{3C} between stations of an array and between components of a station to theoretical phase shifts $a(k, \theta, \xi)$ created over a pre-defined grid of wavenumber k, backazimuth θ and polarization parameters ξ. Backazimuth θ is defined as counter-clockwise from East. Polarization parameters considered are the dip (inclination angle of body waves), the rotation around the x axis (i.e., for differentiating prograde and retrograde Rayleigh waves) and the ellipticity e^B defined in the range [0, 2] with zero referring to a linear horizontal polarization, one referring to a circular polarization and two referring to a linear vertical polarization. We can convert the ellipticity of B3AM to the more standardized definition using.

$$e = H/V = 2 - e^B, e^B \geq 1 \tag{7}$$

$$e = H/V = \frac{1}{e^B}, e^B \leq 1 \qquad (8)$$

Further details about the used code can be found in Löer et al. (2023).

Apart from detrending, demeaning, and removal of instrument response, pre-processing should be kept to a minimum to avoid introducing artificial phase shifts. For the low frequency examples in this study (large station network in Weisweiler and station network in UtahFORGE), some pre-processing is required to obtain stable results for the low-frequency investigation. In these cases, we modify the running-mean time normalization proposed by Bensen et al. (2007), with a total window length equal to the largest period, to simultaneously weigh all three-component waveforms with the same weights calculated using one of the components. This is repeated with weights calculated over each component. Thus, relative amplitudes are always kept the same but spurious signals or earthquakes on each component are reduced in amplitude. No spectral whitening is applied to retain relative amplitudes between components and thus resolve ellipticities. Results from B3AM are normalized per frequency in post-processing to counteract unbalanced energy distributions across the frequencies.

As for all array methods, the wavenumber and frequency limits depend on the station geometry and subsurface velocities. We propose the following steps to determine the input parameters used to calculate the theoretical phase shifts in B3AM.

1. Plot the array response function (Löer et al., 2018) for multiple backazimuths and derive the minimum wavenumber k_{min} as the width of the central peak at half height and the maximum wavenumber k_{max} as the wavenumber where the first peak reaches half the height of the central peak as proposed by Wathelet et al. (2008). We consider k_{min} to represent the resolution limit, that is, the smallest distinguishable wavenumbers, and use a wavenumber minimum of zero in B3AM to allow detection of vertical incident body waves. We found that using $k_{max}/2$ as the upper wavenumber limit works well in keeping the total number of discrete wavenumbers and, thus, the computation time low but obtaining high resolution in the well-resolved wavenumber parts.

2. Derive the desired wavenumber sampling Δk to achieve the desired depth sampling Δr. Since Δk and Δr are inversely related (Equation 1), sampling of r_v is non-linear (Figure 5a). We recommend to severely oversample the wavenumber to artificially increase the radius sampling and reduce the wavenumber sampling through smoothing of the B3AM results in post-processing.

3. Make an educated guess about expected subsurface velocities (v_{min}, v_{max}) in the resolvable depth range estimated using k_{min} and k_{max} in Equation 1.

4. Determine frequency range from wavenumber and velocity range. The minimum frequency $f_{min} = v_{max}k_{min}$ results from the highest expected velocity and the minimum resolvable wavenumber. The maximum frequency $f_{max} = v_{min}k_{max}$ results from the minimum expected frequency and the maximum resolvable wavenumber. Combining these limits defines the resolvable value range (Figure 5b).

5. Determine the desired frequency sampling and time window length for analyses based on the largest Period $T_{max} = \frac{1}{f_{min}}$. We use time window lengths of $4T_{max}$ and windows with 50 % overlap.

In this study, we sample e^B linearly with a spacing of 0.01. This results in equal weighting of horizontal and vertical Rayleigh waves but is different from for example, HVSR curves where the horizontal part is usually sampled higher or exaggerated when plotting. The advantage of linearly sampling e^B is the ease of picking f_e^0. With our chosen e^B sampling, we can resolve H/V amplitudes from 0.01 to 100 with most precision for $H/V < 10$.

B3AM provides wave type, polarization parameters ξ and horizontal wavenumber k_h for every short time window per discrete frequency f. The propagation velocity for Rayleigh waves can be calculated as $v_{ph} = \frac{f}{k_h}$. B3AM results contain velocities outside the expected velocity range due to constant wavenumber sampling (Figure 5b). Thus, we manually exclude results with velocities smaller than v_{min} and larger than v_{max}. We then select only results identified by the polarization parameters as retrograde or prograde Rayleigh waves and calculate two-dimensional histograms of e^B and k_h over f. We smooth the histograms and pick the maximum per frequency and determine the uncertainty as the width of the local peak at half height. Some cases require manual correction of automatic picks which is indicated for the individual results. We calculate $r_v(f) = \frac{1}{2\pi k_h(f)}$ directly from the picked wavenumbers for all frequencies and pick f_p and f_e for all visible modes from the ellipticity curves. We determine the depth of
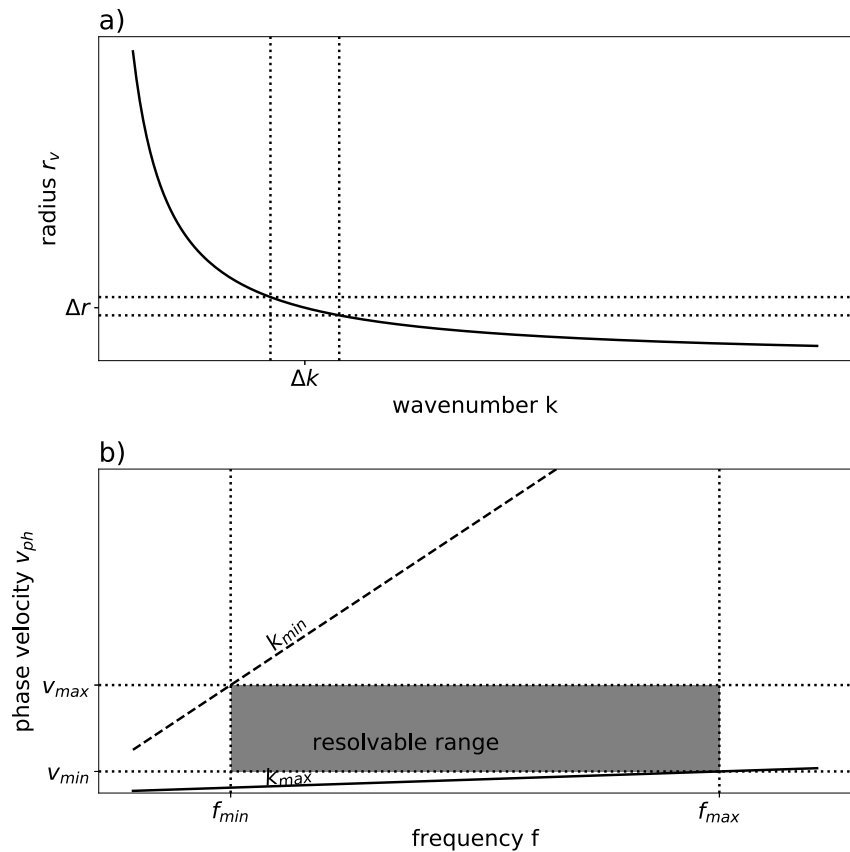
Figure 5. (a) Relation between wavenumber sampling and radius r_v (Equation 5). (b) Relation between wavenumber, frequency and velocity limits and resolvable value range in B3AM.

velocity increases as $d = r_v(f_{p/e})$. Propagating relative errors from the wavenumber histograms, determined as the width at half height of the picked maximum, to the depth estimates directly provides an uncertainty for our depth estimate.

4. Feasibility Test Using Synthetic Waveforms

To validate DARE in a realistic but controlled setting, we computed three-component full-waveform ambient seismic waveforms using a rotated staggered-grid finite-difference scheme (Saenger et al., 2000). The continuous waveforms recorded at the receiver positions described below are available from Finger and Saenger (2023).

The goal of the numerical simulations is a waveform dataset with similar characteristics as observed ambient seismic noise. The main attribute of ambient seismic noise is its seemingly random nature. Waves with different properties arrive from different directions at the receivers. To maximize this randomness, we implement 8,000 randomly located point sources with a Ricker source time function with random origin times, random moment tensor components and random dominant frequencies. We insert these random sources in a three-dimensional velocity model. The inner part of the model, 2.5 times the aperture of the receiver array in the center of the model, is kept free from sources to adhere to the plane wave assumption inherent to the beamforming approach. Frequencies are limited between 0.01 and 2 Hz to avoid numerical dispersion and stability issues. A total of $1{,}540\ s \approx 26$ min of computed waveforms are generated.

The model size is 60 km by 60 km with a total depth of 30 km to allow large wavelengths to exist. The grid spacing is 50 m in all directions and the timestep is 0.005 s, which results in a realistic sampling rate of 200 Hz. The top of the model is a free surface and the sides and the bottom of the model are absorbing boundaries. 441 receivers are distributed in a regular grid of 21 by 21 receivers at the center of the model at the free surface. The inter-receiver

distance is 500 m. We test two velocity models: a) the same velocity as in Figure 1 extended laterally to three dimensions and b) the same velocities as in Figure 1 but with a layer boundary dipping toward the east.

4.1. Velocity Model With Two Horizontal Layers

We apply B3AM to the 26 min of synthetic waveform data recorded with the 100 center receivers and apply the workflow outlined in Section 3 to obtain the maximum wavenumber limit as $\frac{k_{max}}{2} = 0.0001$ m^{-1} and the wavenumber resolution as $\frac{k_{min}}{2} = 3.5 \cdot 10^{-5}$ m^{-1}. We oversample the wavenumber using 200 values. With expected velocities of $v_{min} = 1,000$ m/s to $v_{max} = 5,000$ m/s, the analyzed frequency range is $f_{min} = 0.2$ Hz and $f_{max} = 1$ Hz. The time window length is 20.48 s resulting in 148 total analyzed time windows. The frequency sampling is $\Delta f = 0.0244$ Hz resulting in 32 analyzed frequencies.

The two-dimensional smoothed histograms of $e^B(f)$ (Figures 6a and 6b) and $k_h(f)$ (Figures 6d and 6e) are used to pick multi-mode dispersion and ellipticity curves as the maximum per frequency. We use the width at half height of each local peak as a measure of picking uncertainty and use the relative uncertainty in wavenumber to estimate the uncertainty in velocity (Figure 6f) and radius (Figure 6g). The retrograde ellipticities and wavenumbers can be picked unambiguously. The prograde ellipticities and wavenumbers are picked once the retrograde picks are removed from the prograde histograms. There is some ambiguity between retrograde and prograde waves. However, picked results from B3AM correspond relatively well to those from CPS (Figures 6c and 6f). As expected, the fundamental mode is retrograde and the first higher mode is prograde. Discrepancies in absolute values between B3AM results of the synthetic data and CPS results could stem from uncertainties of the approaches but do not alter the final depth estimates. Picking $f_e^0 = 0.63$ Hz from B3AM and estimating the depth of the sudden velocity change as $r_v^1(f_e^0)$ results in a depth estimate of 973.6 m $\pm$ 356.1 m, a deviation of less than 3% to the true depth.

4.2. Velocity Model With Inclined Layer Boundary

We apply B3AM to the 26 min of continuous synthetic waveform data created with the inclined-layer velocity model. We analyze 100 receivers at a time and then move all receivers one receiver over to analyze the next 100 receivers. In this manner, we analyze a total of 12 subsets of receivers. We use the same parameters for B3AM as for the previous case and estimate the depth of the velocity increase from $r_v^1(f_e^0)$, the half height of the prograde Rayleigh wave energy ellipse at f_e^0, the frequency where the retrograde Rayleigh wave is circular. We determine the uncertainty of $r_v^1(f_e^0)$ from the uncertainty in picking of k^1. We find a good agreement of true and estimated depth across all subarrays (Figure 7) with deviations of less than 10% for half of the subarrays. B3AM seems to generally overestimate the depth in this case. Variations in depth estimate accuracy could result from uncertainty in picking. We only analyzed 32 discrete frequencies. For some cases, differences between subarrays are smaller than the resolution. Additionally, the backazimuth of the Rayleigh waves could influence if the depth is under- or overestimated if the velocity model varies laterally. We investigated the prominent backazimuth for each subarray but could not find a clear correlation to the depth estimate deviation. The footprint of the array, here 4.5 km, does not seem to influence results and depth estimates seem to be an average over the footprint. Therefore, we conclude that the deviation stems mostly from the inherent uncertainties of DARE, such as assuming one-dimensional subsurface velocity structures, being limited in frequency and wavenumber resolution and ambiguity in picking.

5. Application to Recorded Ambient Noise

We apply DARE to two seismic station deployments. At the geothermal test site UtahFORGE in Utah, USA, reflection seismic data show a strong impedance contrast between sediments and the granitoid bedrock (Podgorney, 2020). We use this to validate our approach in a real world scenario. In Western Germany surrounding the town of Eschweiler-Weisweiler, no active seismic surveys have been performed and, thus, geological models (Fritschle et al., 2021) have large uncertainties. Our approach gives the first analysis into the deeper subsurface.

5.1. Application Site UtahFORGE, USA

In December 2016, 49 Fairfield Nodal Zland three-component (3C) geophones were deployed in a regular grid with 600 m inter-station spacing at the geothermal site UtahFORGE in Utah, USA (Pankow, 2016). We analyze 48 hr of continuous waveform data on 20.12.2016 and 21.12.2016 using four subsets of 16 receivers each. This
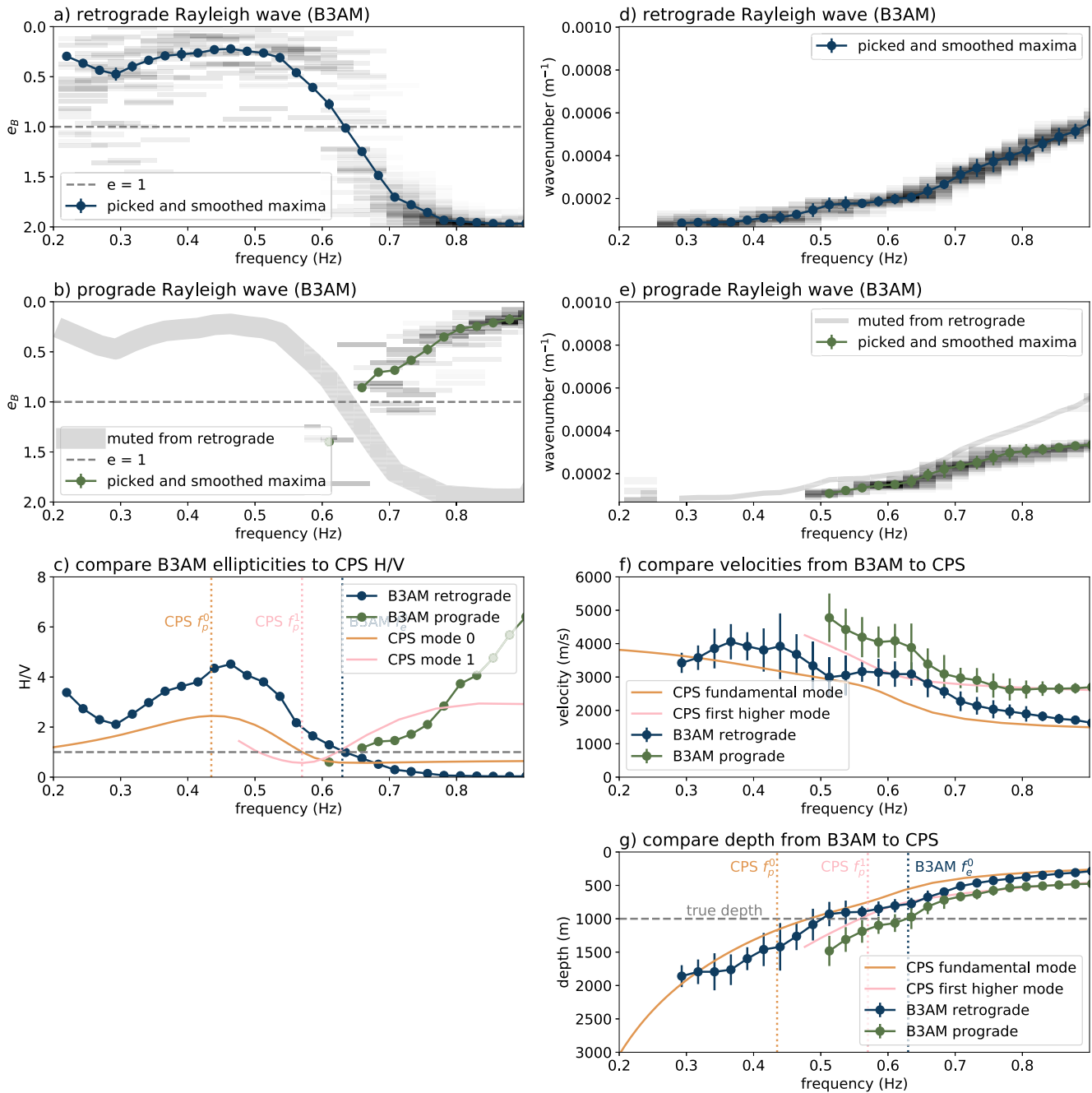
Figure 6. (a) Histogram of $e^B(f)$ for retrograde Rayleigh waves from B3AM and picked and smoothed maxima. Uncertainties are too small to be visible. (b) Histogram of $e^B(f)$ of prograde Rayleigh waves from B3AM and picked and smoothed maxima. (c) Conversion of ellipticities to H/V and comparison to result from CPS. Vertical lines mark frequencies of extrema. (d) Histogram of $k_h(f)$ of retrograde Rayleigh waves from B3AM and picked and smoothed maxima. (e) Histogram of $k_h(f)$ of prograde Rayleigh waves from B3AM. (f) Conversion from wavenumber to velocity and comparison to CPS. (g) Depth estimate of DARE (Equations 1 and 2) applied to results from B3AM and CPS. Vertical lines show frequencies from (c) Horizontal line shows true depth.

timeframe was chosen randomly to not bias results by selecting especially quite times. We restricted the upper wavenumber limit to $k_{max} = 0.0004 \text{ m}^{-1}$ and the frequency range from 0.05 to 0.5 Hz for maximum sensitivity in the expected depth range. Raw waveforms are pre-processed with the modified moving average time normalization as described in Section 3 for more stable results. Ellipticities and wavenumbers showed large uncertainties that made picking challenging. We manually had to revise the automatic picks. The B3AM results for the first 16-receiver subset is shown in Figure 8.
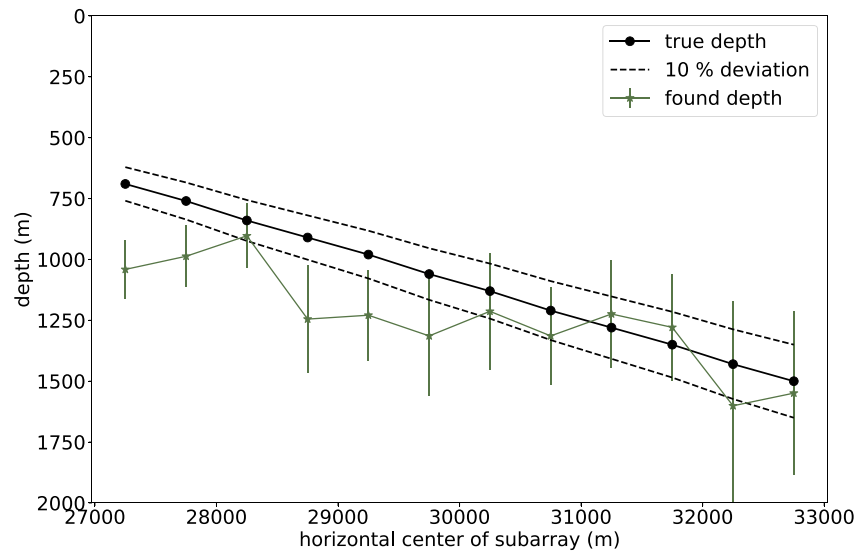
Figure 7. Estimated depth $\left(d^1\left(\mathrm{using}\,f_e^0\right)\right)$ of sudden velocity increase derived using multiple subsets of receivers for the model with an inclined layer boundary.

Comparing the depth estimates from all four 16-receiver subsets to the depth of the granitoid boundary averaged in North-South direction as reported by (Podgorney, 2020) reveals that B3AM recovers the general trend of the inclined boundary well but overestimates the depth significantly (Figure 9). The lower limit of the uncertainty falls within the 50% deviation. The regional velocity model derived from ambient-noise phase velocities and H/V ratios (Wells et al., 2022) reveals an extensive low velocity zone down to depths of about 2 km not taking the elevation into account. Assuming our approach is sensitive to this deeper velocity increase would mean that the deeper velocity increase is sharper than the sediment-to-granitoid boundary at shallower depths. Using estimated velocities from Zhang and Pankow (2021) and typical densities for sandstone and granite, we estimate the shear impedance contrast of the sediment-to-granitoid interface to be $IC = \frac{2630\,\mathrm{kg/m^3}}{2000\,\mathrm{kg/m^3}}\frac{3000\,\mathrm{m/s}}{2000\,\mathrm{m/s}} = 1.97$ and would, thus, be too small for our approach. Thus, we conclude that DARE may confirm a deeper increase in velocities.

5.2. Application Site Weisweiler, Germany

Surrounding the town of Eschweiler-Weisweiler, in the western part of Germany, a small-scale short-term array has been deployed in June 2021 followed by a larger network consisting of among others 27 broadband seismic stations (Finger et al., 2023).

We analyze two hours of continuous waveform data recorded in the night of 20 June 2021 with the small-scale array with B3AM. The small array enables the analysis of wavenumbers up to $k_{max} = 0.023$ m^{-1} in the frequency range of $f_{min} = 1$ Hz to $f_{max} = 4.6$ Hz. B3AM results seem to be sensitive down to frequencies just above the peak frequency of HVSR curves (Figure 10c). This high-filtering effect has been observed in other studies as well (Scherbaum et al., 2003). Thus, the peak frequency of the fundamental mode cannot be resolved well in this case. However, f_e^0 can be clearly identified as 2.44 Hz. The prograde ellipticities have a minimum around 2.8 Hz. In the retrograde and prograde wavenumbers (Figures 10d and 10e), some mode leakage seems to occur. By manually picking modes in restricted frequency ranges allows to estimate the depth as $r_v^1\left(f_e^0 = 2.44\,\mathrm{Hz}\right) = 72.3$ m ± 29.9 m. This is in good agreement with geological models (Fritschle et al., 2021) that estimate a thickness of about 60 m for the quaternary sediments. Using the HVSR peak frequency of 1.6 Hz derived in Gotowik (2022) and the minimal shear velocity of 400 m/s estimated from our B3AM results, we get a depth estimate of $\frac{400\,\mathrm{m/s}}{4\cdot 1.6\,\mathrm{Hz}} = 63$ m using the empirical HVSR equation.

For the large network in Weisweiler, we analyze 48 hr of continuous waveform data recorded at 23 of the broadband stations (Nanometrics Trillium 20 and 120s) that were recording with all components on 16.10.2021 and 17.10.2021. We use a maximum wavenumber limit of $k_{max} = 0.0003$ m^{-1}. We analyze frequencies in the
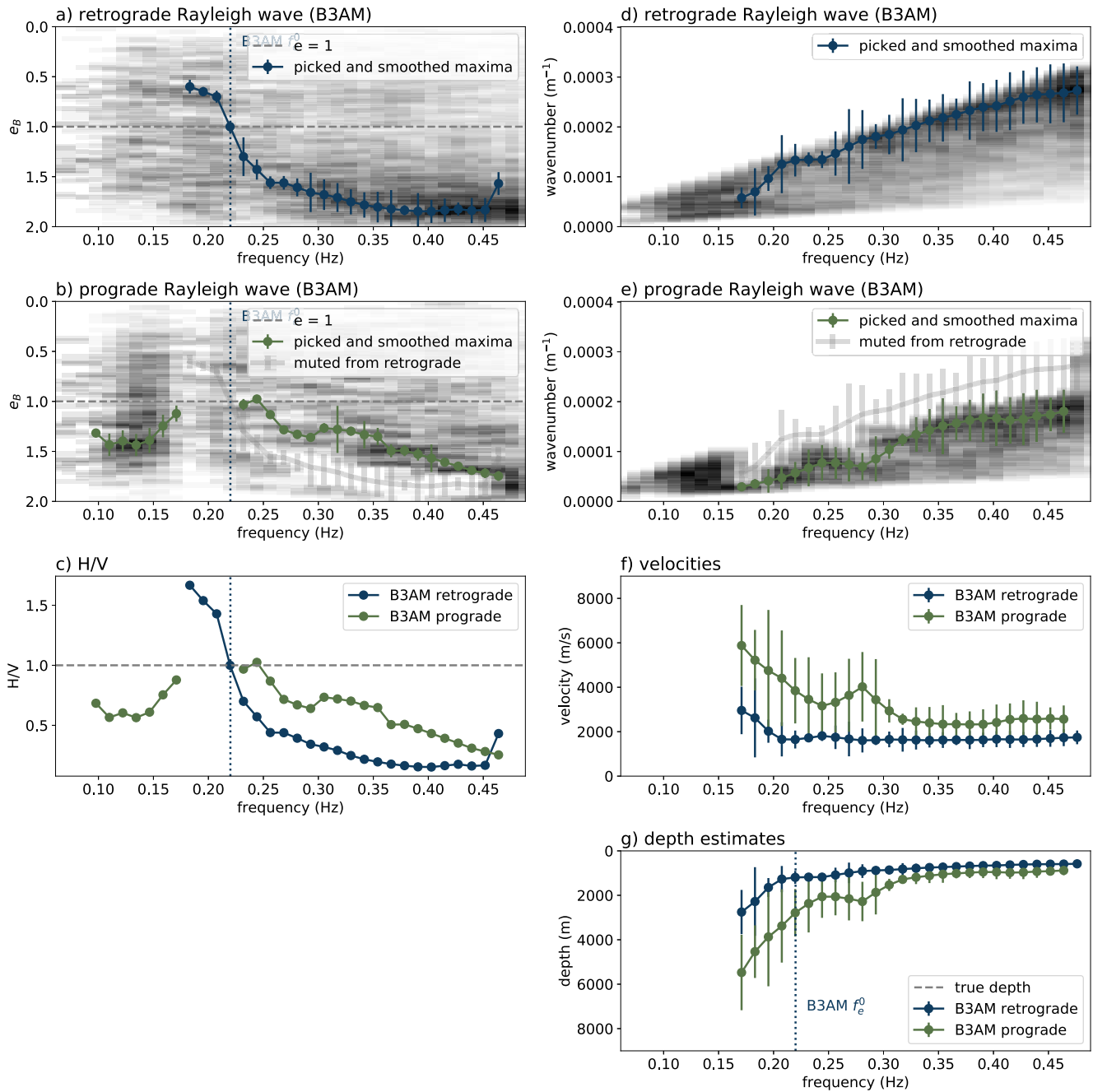
Figure 8. B3AM results of 48 hr of continuous data recorded with the first of four 16-receiver subsets of the Forge array. (a) Ellipticities of retrograde Rayleigh wave, (b) ellipticities of prograde Rayleigh wave, (c) wavenumber of retrograde Rayleigh wave, (d) wavenumber of prograde Rayleigh wave and (e) depth estimate for retrograde and prograde Rayleigh wave.

range of 0.05–0.5 Hz and apply the modified running mean time normalization during pre-processing to get more stable results.

While wavenumbers are well-resolved (Figures 11d and 11e), ellipticities are not well resolved in this case (Figures 11a and 11b). Contrary to the simplified models in previous sections, mostly horizontally polarized ellipses seem to be found for the retrograde wave. However, at around 0.15 Hz the retrograde ellipticities seem to become vertical. If we assume that this is f_e^0, we can estimate a depth as $r_v^1(f_e^0)$ of more than 8 km (Figure 11e). This is deeper than any presently available models. The reported depth of the "Massenkalk" in the geological
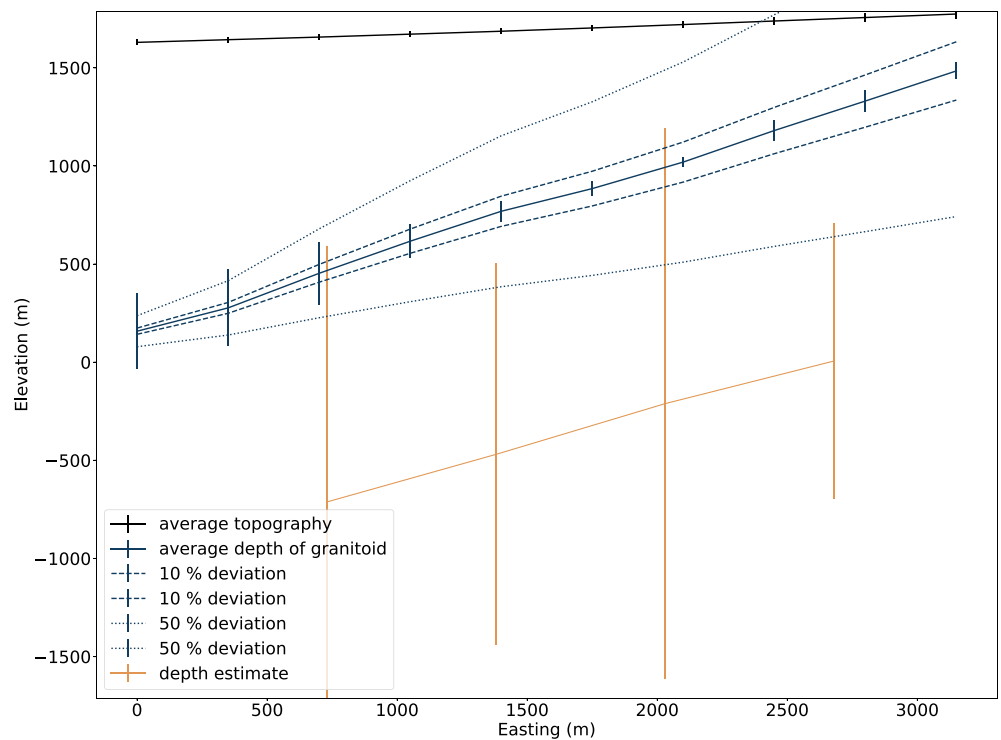
Figure 9. Depth estimates from all four 16-receiver subsets of the FORGE array compared to the topography and depth of the known granitoid boundary averaged in North-South direction.

models in (Fritschle et al., 2021) is about half of that depth. Alternatively assuming that the retrograde ellipticities represent the first higher mode in this case, we can pick $r_v^1(f_p^1) \approx 4\,\mathrm{km}$ but with high uncertainties. We tried to analyze subsets of receivers to observe lateral changes of this depth but uncertainties are too high to make a robust estimate. Similarly as for the case in FORGE, we can conclude that shallower velocity changes have probably too small impedance contrasts for our approach. In this complex geological setting, our simplified approach to estimate the depth of sudden velocity changes might be too simplified to provide a robust estimate.

6. Discussion

We present here a new approach, DARE, to derive the depth of sudden velocity changes from Rayleigh waves recorded at seismic station networks. If ellipticity and phase velocity of Rayleigh waves can be retrieved over the same frequency range, the depth can be estimated as the half height of the energy ellipse at the peak frequencies in ellipticity. DARE has been validated using analytical approximations for a multitude of velocity models. The depth can be estimated within reasonable uncertainties for impedance contrasts above three and different $\frac{v_p}{v_s}$-ratios. In all tested multi-layer models, the strongest impedance contrast is retrieved. DARE is thus best suited to sites with expected large velocity changes, for example, sedimentary basins. DARE can be applied to any seismic recordings containing Rayleigh waves in the interesting frequency range. The prevalence of Rayleigh waves in ambient seismic noise is an advantage for statistically more stable results. In this study, we only applied the method to surface observations but we can envision an application also to borehole stations with an adapted workflow.

Synthetic tests demonstrated the applicability of DARE to realistic data using B3AM to retrieve wavenumber and ellipticity of observed Rayleigh waves. DARE provides more accurate depth estimates than HVSR in the synthetic cases where the ground truth is known. For one-dimensional velocity structures, the synthetic tests predict an increase in accuracy of about 10%. For real-world test cases in frequency ranges where HVSR can also be applied (small array in Weisweiler), the depth estimates of HVSR and DARE are very similar and, thus, can be used jointly. For lower frequencies, where HVSR cannot be applied anymore (large array in Weisweiler and
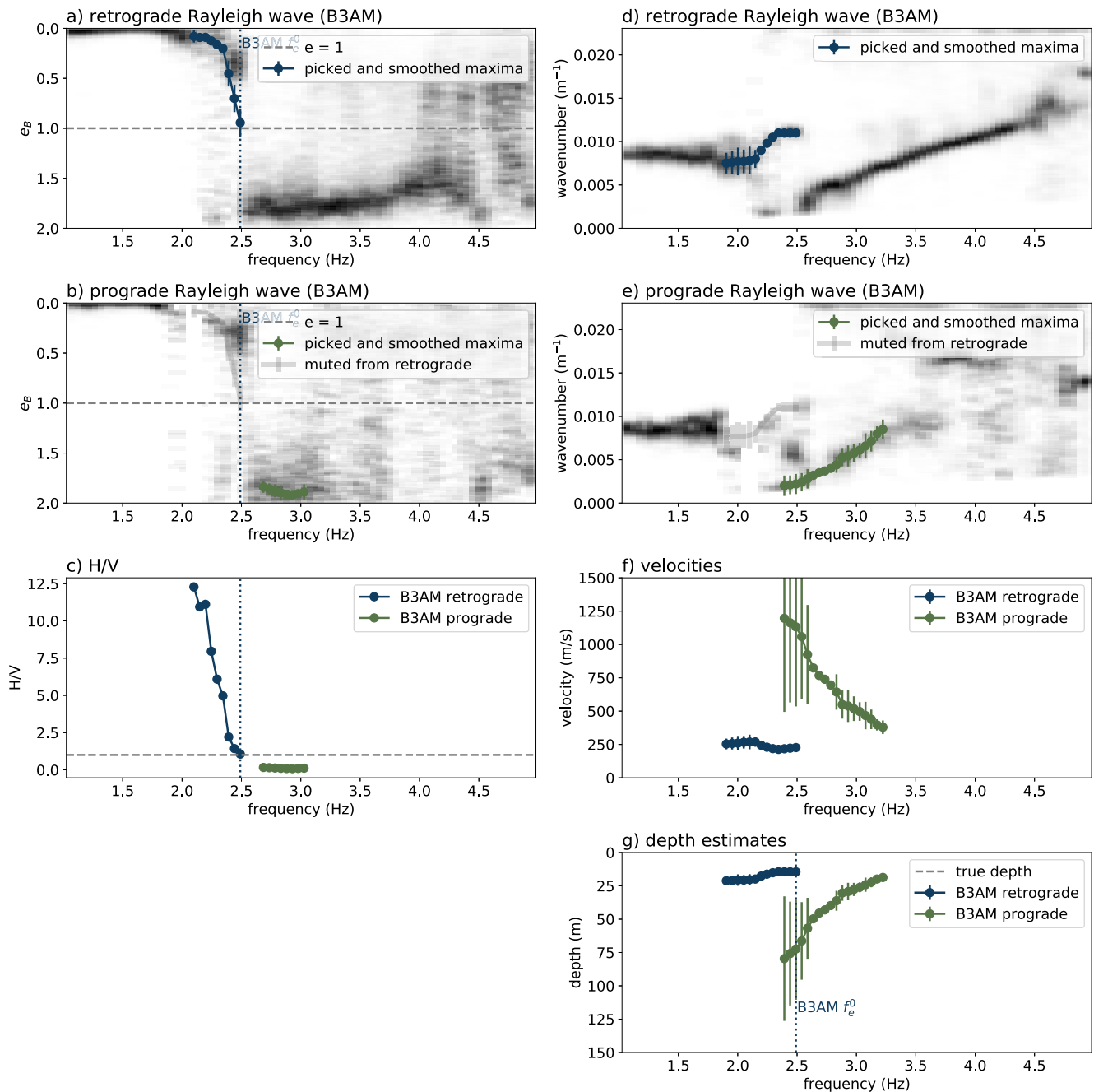
Figure 10. Results of retrograde and prograde Rayleigh waves from B3AM for 2 hours of continuous noise data recorded with the seven stations of the small-scale network. (a) Ellipticities of retrograde Rayleigh wave, (b) ellipticities of prograde Rayleigh wave, (c) wavenumber of retrograde Rayleigh wave, (d) wavenumber of prograde Rayleigh wave and (e) depth estimate for retrograde and prograde Rayleigh wave.

UtahFORGE site), DARE provides a first estimate of the depth of sudden velocity changes. When using overlapping subsets of receivers, the dipping direction can be retrieved as seen in the UtahFORGE case.

Our test cases demonstrate the application of DARE to relatively short recording times. For the synthetic tests (Section 4) 26 min of synthetic data is analyzed in 148 time windows to produce stable results in the used frequency range. For the real-world applications (Section 5), recording times, and, thus, the number of stacked time windows per frequency, needed to be increased for stable results across most frequencies. For the lower frequency applications aiming toward larger depth sensitivity, 48 hr seems to be a reasonable recordings length. This resulted in 2107 time windows for the Forge site and 394 time windows for the Weisweiler site. For the higher
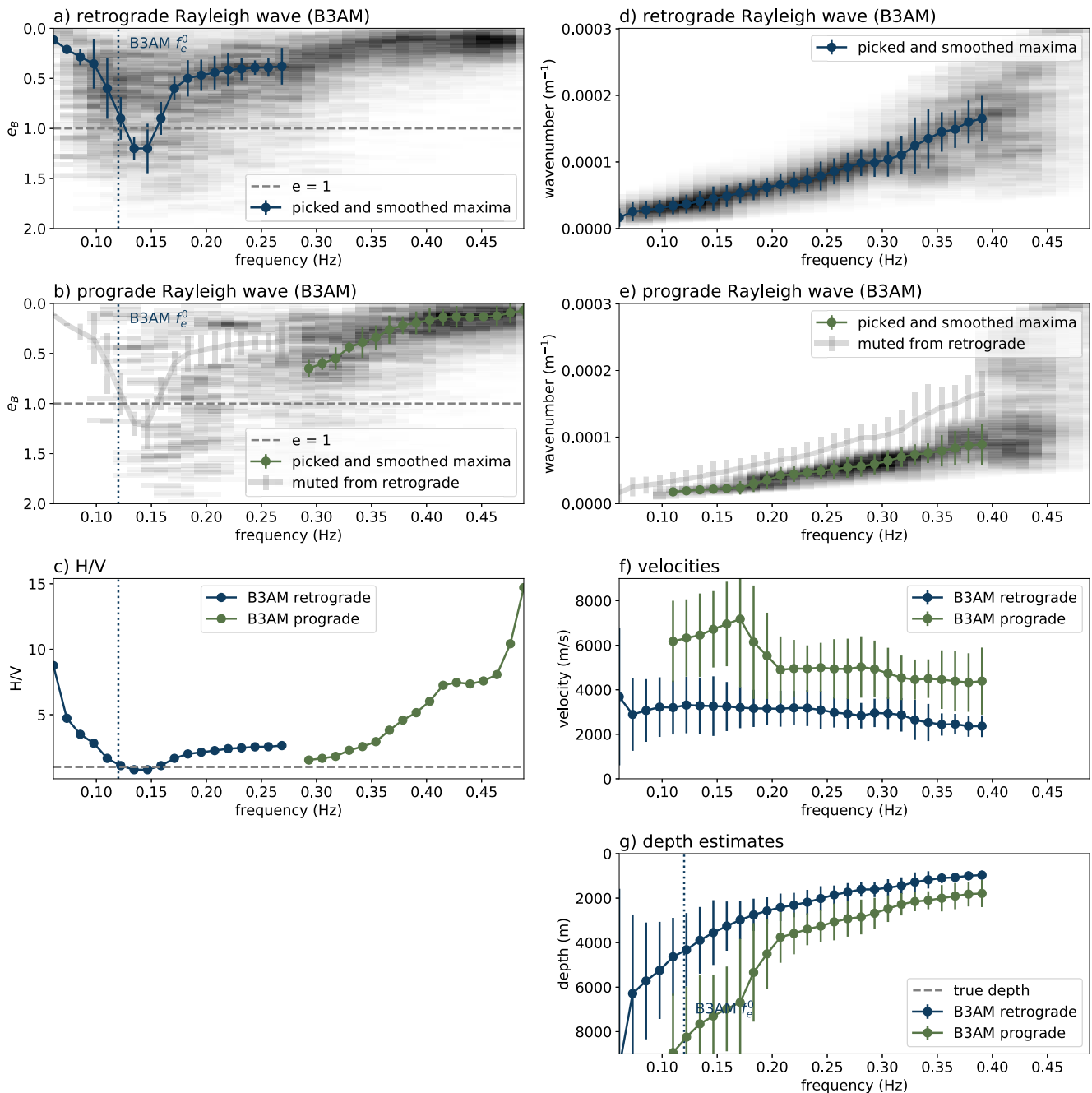
Figure 11. B3AM results of 48 hr of continuous data recorded with 23 stations of the large Weisweiler network. (a) Ellipticities of retrograde Rayleigh wave, (b) ellipticities of prograde Rayleigh wave, (c) wavenumber of retrograde Rayleigh wave, (d) wavenumber of prograde Rayleigh wave, and (e) depth estimate for retrograde and prograde Rayleigh wave.

frequency application at the Weisweiler site, 701 time windows and two hours of recording time were sufficient for stable results. This is slightly more than typical HVSR applications, where recording times are 30 min to 1 hour (Bonnefoy-Claudet et al., 2006), but still a reasonable recording time for rapid measurements. The length of the time windows is determined by the analyzed frequency range. In this study, all time windows overlap by 50%. Increasing this overlap results in more time windows and, thus, could reduce the needed recording time.

We observe that wavenumbers can generally be better resolved than ellipticities using B3AM. This is especially true for the low-frequency, large depth, case sites. This could be due to the assumption of perfect ellipses that are

neither tilted nor distorted. This assumption does not hold true for lower frequencies sensitive to greater depths where velocities cannot be considered homogeneous anymore. Wavenumbers are resolved down to a frequency slightly above the peak frequency of fundamental mode ellipticities. This high-pass filtering effect caused by low-velocity layers overlaying high-velocity layers is a common phenomenon (Scherbaum et al., 2003). The consequence for DARE is that ellipticities of the first higher mode may not be retrieved with enough confidence and, thus, $r_v^1(f_e^0)$ needs to be used to still benefit from the increased accuracy of the first higher mode. However, f_e^0 may introduce slight uncertainties when it is not equal to f_p^1, which can occur when the impedance contrast is small. When only the fundamental mode can be used, the depth estimate is underestimated and the depth estimated can be corrected slightly down. The stronger the impedance contrast, the larger the absolute ellipticity value and thus the factor between the center of the auxiliary circle and the true center of the ellipse is minimal. The large uncertainties in ellipticities, especially for lower frequencies, may be reduced by analyzing more waveform data. Wavenumber uncertainty can be improved with denser station networks. Generally, uncertainties in depth estimates increase with decreasing frequency. With dense enough stations networks and high enough wavenumber sampling, these uncertainties are sufficiently small for an initial estimate of the depth of sudden velocity changes.

The ellipticity e_B in B3AM is linearly resolved between zero and two with higher resolution around $e_B = 1$. This enables the straight-forward identification of f_e^0. At this frequency, mode mis-identification is likely. Identifying f_e^0 thus helps in distinguishing modes and can alleviate some of the challenges in multi-mode dispersion curve analysis (Boaga et al., 2013). Calculating r_v additionally helps to understand the Rayleigh wave behavior in complex velocity models and can give a first estimate of the depth of Rayleigh wave sensitivity. Our proposed approach benefits from multi-mode analysis of Rayleigh waves since depths are over- or underestimated depending on the orientation of the energy ellipse.

When velocity models are not strictly one dimensional, uncertainties can be high since waves arriving from different directions are influenced by different velocities. The resulting one-dimensional depth estimate is an average of velocities over the footprint of the array. The horizontal footprint of this method is a combination of the total used array size and the horizontal size r_h of the Rayleigh wave energy ellipse. We found that in the synthetic test cases, small lateral changes could be resolved by using overlapping subsets of receivers. In UtahFORGE, the general dip could be retrieved using overlapping subsets of receivers but uncertainties remain high.

We see multiple possible uses of DARE:

- Determine osculation frequency (f_e^0) and, thus, aid in preventing mode misidentification when using Rayleigh wave dispersion curves.
- Estimate conversion from frequency to depth for Rayleigh wave phase and group velocity using r_v as an indicator for depth.
- Determine the depth of sudden high-impedance velocity changes for use as constraints in inversions of Rayleigh wave dispersion curves to constrain and validate geological models.
- Combine our approach with HVSR studies for increasing accuracy of shallow velocity structures.
- Use depth of sudden velocity changes to integrate passive and active seismic methods based on common (sub-) horizontal contrasts from both methods.

7. Conclusion

We present a new approach, DARE, to estimate the depth of sudden velocity changes using seismic arrays that generally provides more accurate results than HVSR. DARE is fully self-contained, that is, no information from other studies needed, and does not rely on a priori assumptions about the wavefield. Approximation of the size of the energy ellipse enables a data-driven workflow for initial estimates of the depth of strong impedance contrasts. The capabilities of B3AM to identify and separate wave types from ambient-seismic noise recording enables multi-mode Rayleigh waves to be used in our approach and, thus, significantly increases the depth accuracy. We demonstrated the applicability at two sites in Utah, USA, and in Germany. While high uncertainties remain for the depth of deep velocity changes, DARE shows a high potential to increase accuracy of velocity models on multiple scales.

Appendix A: Additional Analytical Results

Here, we add the plots of phase velocity v_{ph}, ellipticity H/V and depth estimate d^0, d^1 over frequency that were produced using CPS (Herrmann, 2013) and different velocity models. Figure A1 represents the input used to create Figure 3. Figure A2 represents the input used to create Figure 4.
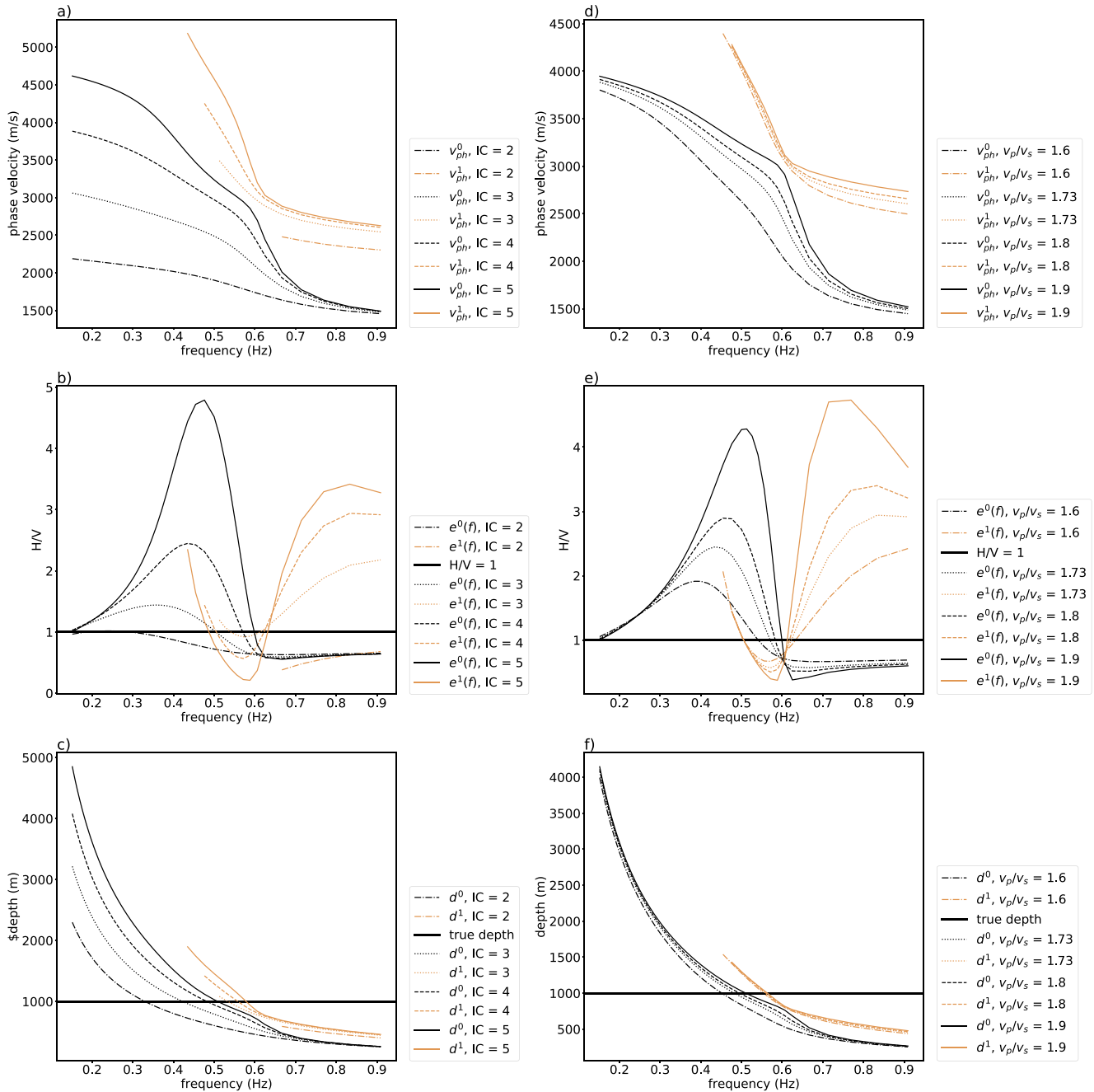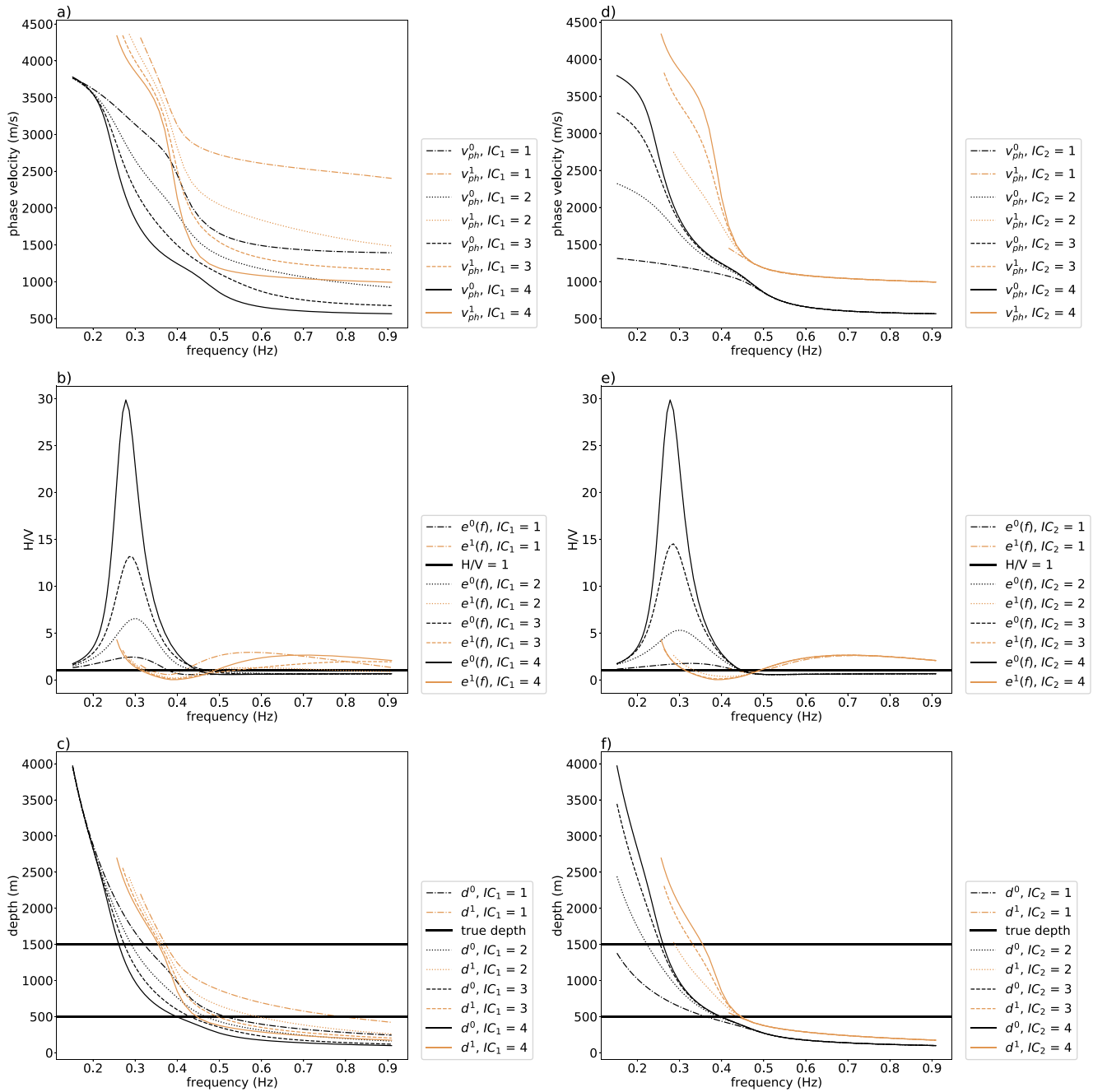

Figure A1. Phase velocity v_{ph}, H/V, and depth estimates (using the complete frequency range and Equations 1 and 2) for different types of theoretical velocity models. In (a) to (c) the impedance contrast IC between two layers is varied. In (d) to (f), the $\frac{v_p}{v_s}$-ratio is varied simultaneously for both layers and the impedance contrast is kept constant at $IC = 4$.

Figure A2. Phase velocity v_{ph}, H/V, and depth estimates (using the complete frequency range and Equations 1 and 2) for different types of theoretical velocity models. In (a) to (c), the impedance contrast of the shallower of two layer boundaries is varied while $\frac{v_p}{v_s} = 1.73$ and $IC = 4$. In (d) to (f), the impedance contrast of the deeper of the two layer boundaries is varied.

Data Availability Statement

The B3AM code for the python version (B3AMpy) used in this study can be downloaded from Finger and Löer (2023). The numerical data created with the rotated staggered-grid finite difference code can be found at Finger and Saenger (2023). The nodal seismic data for Forge is available from (Pankow, 2016) and the depth of the granitoid boundary from (Podgorney, 2020). The passive seismic dataset recorded in Weisweiler, Germany can be obtained from (Finger et al., 2022). A detailed description of this dataset can be found in (Finger et al., 2023).

References

Bard, P. Y., & Team. (2004). Guidelines for the implementation of the H/V spectral ratio technique on ambient vibrations Measurements, processing and interpretations. WP12 European commission - Research general directorate project no. EVG1-CT-2000-0026 SESAME. Report D23(December), 62 pp.

Bensen, G. D., Ritzwoller, M. H., Barmin, M. P., Levshin, A. L., Lin, F., Moschetti, M. P., et al. (2007). Processing seismic ambient noise data to obtain reliable broad-band surface wave dispersion measurements. *Geophysical Journal International*, *169*(3), 1239–1260. https://doi.org/10.1111/j.1365-246X.2007.03374.x

Berg, E. M., Lin, F. C., Allam, A., Qiu, H., Shen, W., & Ben-Zion, Y. (2018). Tomography of Southern California via Bayesian Joint inversion of Rayleigh wave ellipticity and phase velocity from ambient noise cross-correlations. *Journal of Geophysical Research: Solid Earth*, *123*(11), 9933–9949. https://doi.org/10.1029/2018JB016269

Boaga, J., Cassiani, G., Strobbia, C. L., & Vignoli, G. (2013). Mode misidentification in Rayleigh waves: Ellipticity as a cause and a cure. *Geophysics*, *78*(4), EN17–EN28. https://doi.org/10.1190/GEO2012-0194.1

Bonnefoy-Claudet, S., Cotton, F., & Bard, P. Y. (2006). The nature of noise wavefield and its applications for site effects studies. A literature review. *Earth-Science Reviews*, *79*(3–4), 205–227. https://doi.org/10.1016/j.earscirev.2006.07.004

Brenguier, F., Boué, P., Ben-Zion, Y., Vernon, F., Johnson, C. W., Mordret, A., et al. (2019). Train traffic as a powerful noise source for monitoring active faults with seismic interferometry. *Geophysical Research Letters*, *46*(16), 9529–9536. https://doi.org/10.1029/2019GL083438

Fäh, D., Stamm, G., & Havenith, H. B. (2008). Analysis of three-component ambient vibration array measurements. *Geophysical Journal International*, *172*(1), 199–213. https://doi.org/10.1111/j.1365-246X.2007.03625.x

Finger, C., Harrington, R., & Reinsch, T. (2022). The ZB seismic network, 2021–2022 [dataset]. GFZ Data Services. https://doi.org/10.14470/MO7576467356

Finger, C., & Löer, K. (2023). B3AMpy: Beamforming Toolbox for three-component ambient seismic noise [Software]. Fraunhofer Fordatis. https://doi.org/10.24406/fordatis/306

Finger, C., Roth, M. P., Dietl, M., Gotowik, A., Engels, N., Harrington, R. M., et al. (2023). The Weisweiler passive seismological network: Optimised for state-of-the-art location and imaging methods. *Earth System Science Data*, *15*(6), 2655–2666. https://doi.org/10.5194/essd-15-2655-2023

Finger, C., & Saenger, E. (2023). Synthetic ambient seismic noise dataset for testing ambient-noise methods [Dataset]. Fraunhofer Fordatis. https://doi.org/10.24406/fordatis/302

Fritschle, T., Strozyk, F., Oswald, T., Stubbe, H., & Salamon, M. (2021). Deep geothermal energy potential at Weisweiler, Germany: Exploring subsurface mid-palaeozoic carbonate reservoir rocks. *Zeitschrift der Deutschen Gesellschaft fur Geowissenschaften*, *172*(3), 325–338. https://doi.org/10.1127/zdgg/2021/0292

Galetti, E., Curtis, A., Baptie, B., Jenkins, D., & Nicolson, H. (2017). Transdimensional love-wave tomography of the British Isles and shear-velocity structure of the east Irish Sea basin from ambient-noise interferometry. *Geophysical Journal International*, *208*(1), 36–58. https://doi.org/10.1093/gji/ggw286

Gotowik, A. (2022). *Investigating shear velocity profiles and their correlation to local geology in the Lower Rhine Embayment, Germany (Master Thesis)*. Ruhr-Universität Bochum.

Herrmann, R. B. (2013). Computer programs in seismology: An evolving tool for instruction and research. *Seismological Research Letters*, *84*(6), 1081–1088. https://doi.org/10.1785/0220110096

Lin, F. C., Schmandt, B., & Tsai, V. C. (2012). Joint inversion of Rayleigh wave phase velocity and ellipticity using USArray: Constraining velocity and density structure in the upper crust. *Geophysical Research Letters*, *39*(12), 1–7. https://doi.org/10.1029/2012GL052196

Löer, K., Finger, C., Obiri, E., & Kennedy, H. (2023). A comprehensive beamforming toolbox to characterise surface and body waves in three-component ambient noise wavefields. In *Egu general assembly 2023* (pp. EGU23–5670). https://doi.org/10.5194/egusphere-egu23-5670

Löer, K., Riahi, N., & Saenger, E. H. (2018). Three-component ambient noise beamforming in the Parkfield area. *Geophysical Journal International*, *213*(3), 1478–1491. https://doi.org/10.1093/gji/ggy058

Löer, K., Toledo, T., Norini, G., Zhang, X., Curtis, A., & Saenger, E. H. (2020). Imaging the deep structures of the Los Humeros geothermal field, Mexico, using three-component ambient noise beamforming. *Seismological Research Letters*, *91*(6), 3269–3277. https://doi.org/10.1785/0220200022

Nakata, N., Chang, J. P., Lawrence, J. F., & Boué, P. (2015). Body wave extraction and tomography at Long Beach, California, with ambient-noise interferometry. *Journal of Geophysical Research: Solid Earth*, *120*(2), 1159–1173. https://doi.org/10.1002/2015JB011870

Pankow, K. (2016). FORGE nodal array 1 Dataset. International Federation of Digital Seismograph. https://doi.org/10.7914/SN/8J_2016

Picozzi, M., Parolai, S., & Richwalski, S. M. (2005). Joint inversion of H/V ratios and dispersion curves from seismic noise: Estimating the S-wave velocity of bedrock. *Geophysical Research Letters*, *32*(11), 1–4. https://doi.org/10.1029/2005GL022878

Podgorney, R. (2020). Utah FORGE: Earth model mesh data for selected surfaces. Dataset. Retrieved from https://gdr.openei.org/submissions/1107

Saenger, E. H., Gold, N., & Shapiro, S. A. (2000). Modeling the propagation of elastic waves using a modified finite-difference grid. *Wave Motion*, *31*(1), 77–92. https://doi.org/10.1016/S0165-2125(99)00023-2

Scherbaum, F., Hinzen, K. G., & Ohrnberger, M. (2003). Determination of shallow shear wave velocity profiles in the cologne, Germany area using ambient vibrations. *Geophysical Journal International*, *152*(3), 597–612. https://doi.org/10.1046/j.1365-246X.2003.01856.x

Socco, L. V., & Strobbia, C. (2004). Surface-wave method for near-surface characterization: A tutorial. *Near Surface Geophysics*, *2*(4), 165–185. https://doi.org/10.3997/1873-0604.2004015

Toledo, T., Gaucher, E., Jousset, P., Jentsch, A., Haberland, C., Maurer, H., et al. (2020). Local earthquake tomography at Los Humeros geothermal field (Mexico). *Journal of Geophysical Research: Solid Earth*, *125*(12). https://doi.org/10.1029/2020JB020390

Tsai, V. C., Huber, C., & Dalton, C. A. (2023). Towards the geological parametrization of seismic tomography. *Geophysical Journal International*, *234*(2), 1447–1462. https://doi.org/10.1093/gji/ggad140

Wathelet, M., Jongmans, D., Ohrnberger, M., & Bonnefoy-Claudet, S. (2008). Array performances for ambient vibrations on a shallow structure and consequences over vs inversion. *Journal of Seismology*, *12*(1), 1–19. https://doi.org/10.1007/s10950-007-9067-x

Wells, D., Lin, F., Pankow, K., Baker, B., & Bartley, J. (2022). Combining dense seismic arrays and broadband data to image the subsurface velocity structure in geothermally active South-central Utah. *Journal of Geophysical Research: Solid Earth*, *127*(7), 1–42. https://doi.org/10.1029/2022jb024070

Zhang, H., & Pankow, L. K. (2021). High-resolution Bayesian spatial autocorrelation (SPAC) quasi-3-D vs model of Utah FORGE site with a dense geophone array. *Geophysical Journal International*, *225*(3), 1605–1615. https://doi.org/10.1093/gji/ggab049